RESEARCH ARTICLE

Key Points:
- Treatments of soil moisture, texture, and vegetation cover are improved for physically based dust emission scheme
- Dust Fe input to the Southern Ocean is elevated in austral summer
- Majority of atmospheric Fe input into the Southern Ocean comes from sparsely vegetated regions

Supporting Information:
- Supporting Information S1

Correspondence to:
A. Ito,
akinorii@jamstec.go.jp

Do dust emissions from sparsely vegetated regions dominate atmospheric iron supply to the Southern Ocean?

Akinori Ito[1] [iD] and Jasper F. Kok[2] [iD]

[1]Yokohama Institute for Earth Sciences, JAMSTEC, Yokohama, Japan, [2]Department of Atmospheric and Oceanic Sciences, University of California, Los Angeles, California, USA

Abstract Atmospheric deposition of dust aerosols is a significant source of exogenous iron (Fe) in marine ecosystems and is critical in setting primary marine productivity during summer. This dust-borne input of Fe is particularly important to the Southern Ocean, which is arguably the most biogeochemically important ocean because of its large spatial extent and its considerable influence on the global carbon cycle. However, there is large uncertainty in estimates of dust emissions in the Southern Hemisphere and thus of the deposition of Fe-containing aerosols onto oceans. Here we hypothesize that sparsely vegetated surfaces in arid and semiarid regions are important sources of Fe-containing aerosols to the Southern Ocean. We test this hypothesis using an improved dust emission scheme in conjunction with satellite products of vegetation cover and soil moisture in an atmospheric chemistry transport model. Our improved model shows a twofold increase of Fe input into the Southern Ocean in austral summer with respect to spring and estimates that the Fe input is more than double that simulated using a conventional dust emission scheme in summer. Our model results suggest that dust emissions from open shrublands contribute over 90% of total Fe deposition into the Southern Ocean. These findings have important implications for the projection of the Southern Ocean's carbon uptake.

Plain Language Summary Atmospheric deposition of dust aerosols is a significant source of exogenous iron (Fe) in marine ecosystems and is critical in setting primary marine productivity during summer. This dust-borne input of Fe is particularly important to the Southern Ocean, which is arguably the most biogeochemically important ocean because of its large spatial extent and its considerable influence on the global carbon cycle. However, there is large uncertainty in estimates of dust emissions in the Southern Hemisphere and thus of the deposition of Fe-containing aerosols onto oceans. Here we hypothesize that sparsely vegetated surfaces in arid and semiarid regions are important sources of Fe-containing aerosols to the Southern Ocean. We found that open shrubland could be a key contributor to atmospheric soluble Fe input to the Southern Ocean, especially in austral summer. These findings have important implications for the projection of the Southern Ocean's carbon uptake.

1. Introduction

Biological productivity in high-nutrient, low-chlorophyll (HNLC) regions such as the Southern Ocean is often limited by iron (Fe) scarcity [*Martin et al.*, 1990; *Jickells and Moore*, 2015]. Consequently, atmospheric deposition of bioavailable Fe from arid and semiarid regions might modulate primary marine productivity and thus oceanic carbon uptake in these regions during summer [*Boyd et al.*, 2010; *Conway et al.*, 2015; *Winton et al.*, 2016]. However, significant uncertainties remain regarding the magnitude of the dust emissions and thus the effect of dust deposition on the oceans, especially in the Southern Hemisphere (SH) [*Shao et al.*, 2011; *Schulz et al.*, 2012; *Hajima et al.*, 2014]. The major source regions of atmospheric Fe to the Southern Ocean include southern South America (Patagonia), Australia, and southern Africa [*Mahowald,* 2007; *Li et al.*, 2008; *Johnson et al.*, 2010; *Ito and Shi*, 2016]. Large parts of these regions are (sparsely) vegetated, which causes dust emissions to be highly spatially variable and particularly susceptible to climate and land use changes, further enhancing the relevance of Southern Hemispheric dust emissions to ecosystems and climate change [*McConnell et al.*, 2007; *Bhattachan et al.*, 2012; *Bhattachan and D'Odorico*, 2014]. Specifically, the loss of ecosystem services (e.g., grazing, biomass burning, and climate change) may alter the grassland to shrub dune land, release the suppression of dust emission due to the vegetation, and thus increase the susceptibility of areas to soil erosion [*Ravi et al.*, 2012; *D'Odorico et al.*, 2013; *Webb et al.*, 2014]. Potentially, expanded source regions include dune fields after fires in southern South America, Australia, and southern Africa [*Bullard et al.*, 2008]. Moreover, fires in shrublands may change the physical and chemical properties of Fe-containing minerals both under shrub canopy and the shrub interspaces [*Kavouras et al.*, 2012].

A common approach to parameterize the spatial variability of dust emissions is the use of a preferential source function, as pioneered by *Ginoux et al.* [2001] based on the idea that topographic depressions are particularly prolific dust sources [*Prospero et al.*, 2002]. The *Ginoux et al.* [2001] source function has been widely used and evaluated in atmospheric chemistry transport models [e.g., *Fairlie et al.*, 2010; *Johnson et al.*, 2010; *Ito et al.*, 2012], although the concept that topographic depressions dominate dust emissions has been disputed [e.g., *Mahowald and Dufresne*, 2004; *Schepanski et al.*, 2009]. The original *Ginoux et al.* [2001] source function only classified bare ground as a possible dust source, while the more recent study of *Ginoux et al.* [2012], which used the Moderate Resolution Imaging Spectroradiometer Deep Blue (MODIS DB) product to derive a source function, estimated that 20% of dust is emitted from vegetated surfaces. This substantial contribution from vegetated regions is qualitatively consistent with field measurements, which show that dry lands with sparse vegetation can emit significant amounts of dust from the gaps between the vegetation cover [*Okin and Gillette*, 2001]. In fact, measurements and physically explicit sediment transport models suggest that current climate model parameterizations underestimate dust fluxes from sparsely vegetated regions [*Okin*, 2008; *Li et al.*, 2013].

In addition to these possible problems in capturing dust emissions from sparsely vegetated regions, the source function does not account for temporal variability in dust emissions. These are critically dependent on both changes in wind speed and in the threshold wind friction velocity at which dust emission is initiated. Although this threshold depends on a variety of factors, including soil size distribution and mineralogy, measurements indicate that it is particularly sensitive to soil moisture [*Fécan et al.*, 1999; *Ishizuka et al.*, 2008]. Moreover, recent modeling studies suggest that the dust flux is more sensitive to the threshold wind friction velocity, and thus to soil moisture content, than accounted for in conventional models [*Kok et al.*, 2014a, 2014b; *Gherboudj et al.*, 2015; *Haustein et al.*, 2015].

These problems of representing the spatial and temporal variability of dust emissions in global models, especially in the SH, could be partially addressed by describing the spatial and temporal variability of parameters used in physically based dust emission schemes from remote sensing data. Indeed, satellite-based estimates of fractional vegetation area in conjunction with land cover type are already used to parameterize biomass burning and biogenic emissions of volatile organic compounds [e.g., *Ito and Penner*, 2004; *Ito*, 2011; *Guenther et al.*, 2012] and could be similarly used to account for suppressing effects of vegetation on dust emission [e.g., *Chappell et al.*, 2010; *Vest et al.*, 2013; *Webb et al.*, 2014]. In addition, despite limitations on current satellite-based estimates of soil moisture, remote sensing data have considerable potential for parameterizing the effects of soil moisture on dust emissions [*Gherboudj et al.*, 2015].

The variability of dust emissions can be also affected by long-term changes in the soil surface properties. In particular, the climate change and land use dynamics may alter physical and chemical properties of the soils [*D'Odorico et al.*, 2013]. As in the case of Australian deserts, weak dust activity compared to the Northern Hemisphere (NH) might be associated with geologically old and weathered soils [*Prospero et al.*, 2002]. The changes in soil texture can affect the capability of the soil to emit dust aerosols through saltation processes, which result in partial destruction of soil aggregates [*Kok*, 2011]. In saltation, this capability is primarily controlled by the abundance of fine particles within the soil [*Marticorena and Bergametti*, 1995; *Shao*, 2008; *Kok et al.*, 2012]. In particular, a positive relationship was observed between the ratio of the vertical dust flux to the horizontal saltation flux against the clay content for the soils having less than the soil clay fraction of 0.2 [*Marticorena and Bergametti*, 1995]. Conversely, a negative correlation was observed between the soil sand content and emitted dust flux [*Sweeney and Mason*, 2013]. Thus, many dust emission schemes assumed that dust emission increases with the clay content of the soil [*Marticorena and Bergametti*, 1995; *Zender et al.*, 2003; *Kok et al.*, 2014a]. However, recent observations suggest that sand dunes, which have low clay content, might be a substantial source of dust [*Crouvi et al.*, 2012], suggesting that scaling dust emissions with soil clay content could underestimate the emissions from sandy soils.

Here we hypothesize that sparsely vegetated surfaces in arid and semiarid regions are substantial sources of Fe to the Southern Ocean. To test this hypothesis, we use an atmospheric chemistry transport model to estimate atmospheric Fe supply to the oceans. We improve the accuracy of these simulations by (i) implementing a physically based parameterization for dust emission [*Kok et al.*, 2014a], (ii) incorporating suppression of dust emission due to vegetated areas into this dust emission scheme, (iii) using satellite products to describe spatial and temporal variability in soil moisture and vegetation cover, and (iv) improving the

parameterized dependence of dust emissions on soil texture. After evaluating the model output against observations of aerosol optical properties near dust source regions, we found that open shrubland could be a key contributor to atmospheric soluble Fe input to the Southern Ocean, especially in austral summer.

2. Model Approach

Since, unlike the NH, the SH lacks large barren lands for the dust sources, dust emissions from partially vegetated regions might be considerably important for the SH than the NH. We thus test the hypothesis that relatively vegetated regions contribute a large fraction of the deposited Fe to the Southern Ocean, using five different numerical experiments with the atmospheric chemistry transport model (Table 1). The first experiment used the dust emission scheme of *Ginoux et al.* [2001] (Experiment 1), whereas the other four experiments used the physically based dust emission scheme of *Kok et al.* [2014a] to properly simulate seasonal changes (Experiments 2–5). We further examined satellite products for the latter scheme to describe the soil moisture and surface vegetation cover (Experiments 3–5).

2.1. Model Description

This study uses the Integrated Massively Parallel Atmospheric Chemical Transport model [*Rotman et al.*, 2004; *Liu et al.*, 2005; *Feng and Penner*, 2007; *Ito et al.*, 2007, 2009, 2012, 2014, 2015; *Lin et al.*, 2014; *Xu and Penner*, 2012; *Ito*, 2015; *Ito and Shi*, 2016]. The model is driven by assimilated meteorological fields from the Goddard Earth Observation System (GEOS) of the NASA Global Modeling and Assimilation Office with a horizontal resolution of 2.0° × 2.5° and 59 vertical layers. The model simulates the emissions, chemistry, transport, and deposition of major aerosol species and their precursor gases [*Liu et al.*, 2005; *Feng and Penner*, 2007; *Ito et al.*, 2007, 2009, 2012, 2014, 2015; *Lin et al.*, 2014; *Xu and Penner*, 2012; *Ito*, 2015]. The model-calculated concentrations of total and soluble Fe in aerosols have been extensively compared with field observations [*Ito and Feng*, 2010; *Ito*, 2012, 2013, 2015; *Ito and Xu*, 2014; *Ito and Shi*, 2016].

Our model uses the mineralogical map for Fe content in soils [*Journet et al.*, 2014], as was described in *Ito and Shi* [2016]. The mineral dust (biomass burning) aerosols are emitted with the initial Fe solubility of 0.1% (0%) [*Ito*, 2015; *Ito and Shi*, 2016]. Subsequently, aging processes for Fe-containing aerosols are dynamically simulated for the size-segregated dust and combustion aerosols in the model, accounting for the formation of soluble Fe in aerosol water due to proton-promoted, oxalate-promoted, and photo-reductive Fe dissolution schemes [*Ito*, 2015; *Ito and Shi*, 2016]. While the Fe dissolution scheme for mineral dust was developed using laboratory measurements for Saharan dust samples, the calculation (blue triangles) reproduced the Fe release from Australian dust aerosols in acidic solution (Figure S1 in the supporting information) [*Mackie et al.*, 2005; *Ito and Xu*, 2014; *Ito and Shi*, 2016]. It should be noted that the Fe dissolution rates from mineral dust are much slower than those from combustion aerosols (red circles) [*Chen and Grassian*, 2013; *Ito*, 2015].

To improve the accuracy of our simulations of soluble Fe deposition to the Southern Ocean, we made several upgrades to the deposition schemes used in *Ito and Shi* [2016]. Specifically, we adopted a semiempirical parameterization for below-cloud scavenging of size-resolved aerosols by rain and snow [*Wang et al.*, 2014], and a correction for the fractional area distribution between in-cloud and below-cloud scavenging [*Wang et al.*, 2011]. To improve the accuracy of aerosol optical depth (AOD) estimates, we updated the biogenic emission schemes for isoprene and monoterpenes from that used in *Ito et al.* [2009] to the Model of Emissions of Gases and Aerosols from Nature version 2.1 [*Guenther et al.*, 2012]. We used the assimilated meteorological data of surface air temperature and photosynthetic active radiation (direct and diffuse) to account for the variations associated with temperature and solar radiation, following *Palmer et al.* [2006]. We obtained the 8 day MODIS leaf area index (LAI) map at 500 m to simulate seasonal variations in leaf biomass and age distribution [*Myneni et al.*, 2015]. The average LAI for vegetated areas was estimated by dividing the grid average LAI by the fraction of the grid that is covered by vegetation [*Guenther et al.*, 2012]. We used the MODIS vegetation continuous fields (VCF) at 250 m to calculate the fraction of the vegetated areas over the lands [*DiMiceli et al.*, 2011]. The total isoprene (monoterpenes) emission from terrestrial vegetation was 480 Tg C yr^{-1} (80 Tg C yr^{-1}).

2.2. Mineral Dust Emission Schemes

For the base simulation of mineral aerosols (Experiment 1), we used the model's default dust emission scheme, which was described in *Ito et al.* [2012]. This scheme used the dust emission scheme of *Ginoux*

Table 1. Summary of Five Simulations Performed in This Study

Simulation	Emission Scheme	Soil Moisture	Soil Map	Vegetation Effect
Experiment 1	*Ginoux et al.* [2001]	Model	Not Used	Not Used
Experiment 2	*Kok et al.* [2014a]	Model	Clay and Silt[a]	*Webb et al.* [2014][c]
Experiment 3	*Kok et al.* [2014a]	Satellite	Clay and Silt[a]	*Webb et al.* [2014][c]
Experiment 4	*Kok et al.* [2014a]	Satellite	Clay[b]	*Webb et al.* [2014][c]
Experiment 5	*Kok et al.* [2014a]	Satellite	Clay and Silt[a]	*Li et al.* [2013][d]

[a]The dust emission is scaled by the clay and silt content of the soil using equations (13) and (14).
[b]The dust emission is scaled by The clay content of the soil using equations (10)–(12).
[c]Suppression of dust emission due to vegetation is accounted for using equations (15) and (16). We fit an exponential function to the data set from *Webb et al.* [2014].
[d]Suppression of dust emission due to vegetation is accounted for using equation (17). We fit an exponential function to the data set from *Li et al.* [2013].

et al. [2001] for the bare ground at $1.0° \times 1.0°$ resolution, which was estimated from the advanced very high resolution radiometer (AVHRR). The dust emission flux, E_d, is given by

$$E_d = C_d \times S_d \times u_{10m}^2 \times (u_{10m} - u_t), (u_{10m} > u_t),\qquad(1)$$

where C_d is a global scaling constant for dust emissions, S_d is the source function, $u_{10\,m}$ is the horizontal wind speed at 10 m, and u_t is the threshold wind velocity. The dust emissions are completely shut off (i.e., $u_t = 100\,\mathrm{m\,s^{-1}}$) in the case of wet soil where the surface soil wetness of the meteorological data set, θ_{met}, exceeds 0.5, which is much higher than the typical value of θ_{met} in arid regions [*Ginoux et al.*, 2001]. Experiment 1 provides a reference value for a bare and dry surface, because the threshold wind velocity is hardly sensitive to the soil wetness in arid regions [*Ginoux et al.*, 2001] (equation (3)).

In addition to the base simulation, we performed four simulations with the new physically based dust emission scheme of *Kok et al.* [2014a] (Experiments 2–5). In this scheme, the dust emission flux is given by

$$E_d = C_{tune} \times \exp\left(-C_a \times \frac{u_{*st} - u_{*st0}}{u_{*st0}}\right) \times F_{bare} \times \frac{\rho_a \times \left(u_*^2 - u_{*t}^2\right)}{u_{*st}} \times \left(\frac{u_*}{u_{*t}}\right)^\beta \times \gamma, \left(u_* > u_{*t}\right),\qquad(2)$$

where

$$\beta = C_\beta \times \frac{u_{*st} - u_{*st0}}{u_{*st0}},\qquad(3)$$

and C_{tune} is a global scaling factor for dust emissions, F_{bare} is a function of the nonvegetation cover, and ρ_a is the air density. The parameter γ scales the horizontal sand flux to the vertical dust flux. The soil friction velocity, u_*, is defined from the wind stress on the bare erodible soil [*Zender et al.*, 2003; *Kok et al.*, 2014a], and u_{*t} denotes the soil threshold friction velocity above which dust emission occurs. Furthermore, u_{*st} is the standardized threshold friction velocity at standard atmospheric density, $\rho_{a0} = 1.225\,\mathrm{kg\,m^{-3}}$:

$$u_{*st} \equiv u_{*t} \times \sqrt{\frac{\rho_a}{\rho_{a0}}},\qquad(4)$$

u_{*st0} is the minimal value of u_{*st} for an optimally erodible soil ($u_{*st0} \approx 0.16\,\mathrm{m\,s^{-1}}$), $C_\alpha = 2.0 \pm 0.3$, and $C_\beta = 2.7 \pm 1.0$. Since the dust flux increases exponentially with a decrease in the standardized threshold friction velocity, u_{*st}, the dust flux is substantially more sensitive to the soil moisture than is the case for Experiment 1.

2.3. Accounting for Effect of Soil Moisture on Dust Emission

We use the *Fécan et al.* [1999] parameterization to account for the effect of soil moisture on the soil threshold friction velocity, u_{*t}. This parameterization uses an empirical relationship between soil's clay fraction, f_{clay}, and threshold gravimetric soil moisture content, w_t, above which soil moisture will quickly increase the threshold friction velocity:

$$w_t = 0.17 \times f_{clay} + 0.14 \times f_{clay}^2. \tag{5}$$

The threshold gravimetric soil moisture content thus increases rapidly with clay fraction and is around 0.02 (g g^{-1}) for a typical soil clay fraction of 0.1. However, the soil moisture content often exceeds 0.02 (g g^{-1}) over active dust emission regions in global climate models and reanalysis products [*Zender et al.*, 2003]. Thus, the *Fécan et al.* [1999] parameterization can effectively eliminate dust emissions from the source regions when it is applied to the modeled soil moisture content under wetter conditions.

Evaluation of soil moisture products with in situ observations over semiarid areas in southeastern Arizona during summer months (July–September) showed that climate models and reanalysis products had large positive biases (>0.1 m^3 m^{-3}), while satellite products had low biases (a median value of 0.0056 m^3 m^{-3}) [*Stillman et al.*, 2016]. We thus use remote sensing data to more realistically implement the Fécan et al. parameterization in Experiments 3–5, whereas Experiment 2 uses the assimilated meteorological data of soil wetness (or fractional degree of saturation). Specifically, we corrected the biases in the meteorological data using monthly observational data, θ_{obs} (X, Y, T), from the Tropical Rainfall Measuring Mission Microwave Imager (TMI) between about 38° north and south latitude [*Owe et al.*, 2008]. For the region outside of the satellite coverage, we used the observational data from the Advanced Microwave Scanning Radiometer on the Earth Observing System (EOS) Aqua satellite (AMSR–E) [*Owe et al.*, 2008]. The moisture retrievals were made with a radiative transfer-based land parameter retrieval model [*Owe et al.*, 2008]. We thus obtain the modeled soil wetness, θ_{mod} (X, Y, t), by correcting the bias in the soil wetness of the assimilated meteorological data set at each time step, θ_{met} (X, Y, t):

$$\theta_{mod}(X, T, t) = \theta_{met}(X, Y, t) - \theta_{bias}(X, Y, T), \tag{6}$$

where the bias between the assimilated soil wetness and the remotely sensed soil wetness, θ_{bias} (X, Y, T) is given by the following:

$$\theta_{bias}(X, Y, T) = \theta_{met}(X, Y, T) - \theta_{obs}(X, Y, T). \tag{7}$$

We convert the fractional degree of saturation (dimensionless), θ_{mod} (X, Y, t), to the volumetric soil moisture θ (m^3 m^{-3}) to be used in the Fécan et al. parameterization after unit conversion by the following:

$$\theta(X, Y, t) = \theta_{mod}(X, Y, t) \times \theta_s(X, Y), \tag{8}$$

where the saturated soil moisture (or saturation ratio), θ_s (X, Y), decreases with increasing sand mass fraction, F_{sand}, in the soil [*Zender et al.*, 2003].

$$\theta_s(X, Y) = 0.489 - 0.126 \times F_{sand}. \tag{9}$$

The mass fractions of clay, silt, and sand in soils are taken from global database of soil minerals [*Nickovic et al.*, 2012]. After using equation (8) to obtain the volumetric soil moisture, the model uses it to obtain the gravimetric soil moisture content (g g^{-1}) [*Zender et al.*, 2003] that is needed to calculate the dust emission threshold [*Fécan et al.*, 1999] (equation (15)).

2.4. Accounting for Effect of Soil Texture on Dust Emission

We examine effect of soil texture on dust emission, γ, with two different functions to present improved results from the conventional parameterization, which uses the scaling of γ with soil clay content [*Kok et al.*, 2014a]. For Experiment 4, we take the following equations for γ:

$$\gamma = 0.05, \qquad (F_{clay} < 0.05), \tag{10}$$

$$\gamma = F_{clay}, \qquad (0.05 \leq F_{clay} \leq 0.2), \tag{11}$$

$$\gamma = 0.2, \ (F_{clay} > 0.2). \tag{12}$$

These values of γ (0.05 and 0.2) for clay content less than 0.05 and larger than 0.2, respectively, are based on *Crouvi et al.* [2012] and *Marticorena and Bergametti* [1995]. In addition to the scaling of γ with clay content (equations (10)–(12)), we perform three simulations of Experiments 2, 3, and 5 in which we instead use the following equations for γ:

Table 2. Annual Fe Emission for Dust (Tg Fe yr^{-1}) in SH, NH, and Total Lands From Five Simulations[a]

Simulation	Emissions in SH	Emissions in NH	Total Emissions
Experiment 1	7.9	108	115
Experiment 2	7.0 (75%)	96 (7%)	103 (12%)
Experiment 3	13 (86%)	104 (11%)	117 (20%)
Experiment 4	15 (85%)	105 (13%)	120 (22%)
Experiment 5	13 (90%)	102 (9%)	115 (18%)

[a]The numbers in parentheses represent the fractional contribution (percentage) of dust emissions originating from land cover type classified as open shrublands to the sum of those from barren and open shrublands. Note that only land surface classified as bare ground at a one-by-one degree was considered as possible dust source region in Experiment 1.

$$\gamma = \frac{1}{1 + (0.4 - F_{clay}) - F_{silt}}, \quad (F_{clay} < 0.2), \tag{13}$$

$$\gamma = \frac{1}{1 + F_{clay} - F_{silt}}, \quad (F_{clay} \geq 0.2). \tag{14}$$

The dust emission flux thus increases with clay and silt content in Experiments 2, 3, and 5 but decreases with clay content when $F_{clay} \geq 0.2$ at constant silt content. This alternative scaling is based on the field experimental results of *Gillette* [1977], *Mikami et al.* [2005], and *Sweeney and Mason* [2013]. The latter two studies showed that the dust emission flux increased with content of silt-sized particles in soils due to the breakup of clay-silt aggregates, even though the differences in clay content were small. Thus, it is intended to account for the observation that fine particles released into the atmosphere increase with fine particles in parent soils, while excess clay fraction increases the resistance of soil aggregates to fragmentation, thereby reducing dust emissions.

2.5. Accounting for Effect of Surface Vegetation Cover on Dust Emission

For each model grid box, the modeled dust emission flux is the sum of the fluxes produced by the various surface types, weighted by their fractional occurrence in the grid box, f_{land}. To achieve this, we used the MODIS land cover map at 500 m resolution to calculate the fraction of barren and open shrublands in each model grid box [*Friedl et al.*, 2010]. The International Geosphere-Biosphere Programme land cover type classification defines barren lands as lands of exposed soil, sand, rocks, or snow that never have more than 10% vegetated cover during any time of the year. Open shrublands are defined as lands with woody vegetation less than 2 m tall and with shrub canopy cover between 10 and 60%. The fractional snow cover is derived from the water equivalent snow depth provided by the meteorological data set [*Zender et al.*, 2003]. Within each 500 m grid, we used the MODIS VCF at 250 m to calculate the fraction of the grid cell that is nonvegetated and thus capable of emitting dust aerosols in barren and open shrublands, f_{bare} (i.e., bare ground area divided by total land area, S_{bare}/S_{land}) [*DiMiceli et al.*, 2011]. The fractional vegetation cover was estimated by summing the fraction of tree and grass cover in barren lands and open shrublands, respectively.

Any types of roughness elements (e.g., living and dead plants) decrease the susceptibility to wind erosion of the bare soil [*Fryrear*, 1985; *Vest et al.*, 2013]. Therefore, satellite retrievals of the fractional vegetation cover could be used to represent the fractional cover by such roughness elements. Here we examine two exponential functions to estimate vegetation cover levels for controlling erosion (hereinafter vegetation threshold), based on field experimental studies [*Li et al.*, 2013; *Webb et al.*, 2014]. The study of *Webb et al.* [2014] showed that, at the plot scale (i.e., 50 m × 50 m), the aeolian horizontal sediment flux, which was simulated with the physically explicit shear stress distribution model of *Okin* [2008], exhibits threshold-type responses to bare ground cover. To apply the vegetation threshold to the large-scale model in Experiments 2–4, we fit an exponential function to the data set (Figure S2a):

$$F_{bare} = f_{bare} \times f_{land}, \quad (f_{bare} \geq 0.7), \tag{15}$$

$$F_{bare} = C_a \times \exp(-C_b \times f_{bare}) \times f_{land}, (f_{bare} < 0.7, R^2 = 0.59), \tag{16}$$

where f_{bare} is the nonvegetated fraction for each 250 m cell, $C_a = 0.00555$, and $C_b = 6.9$.
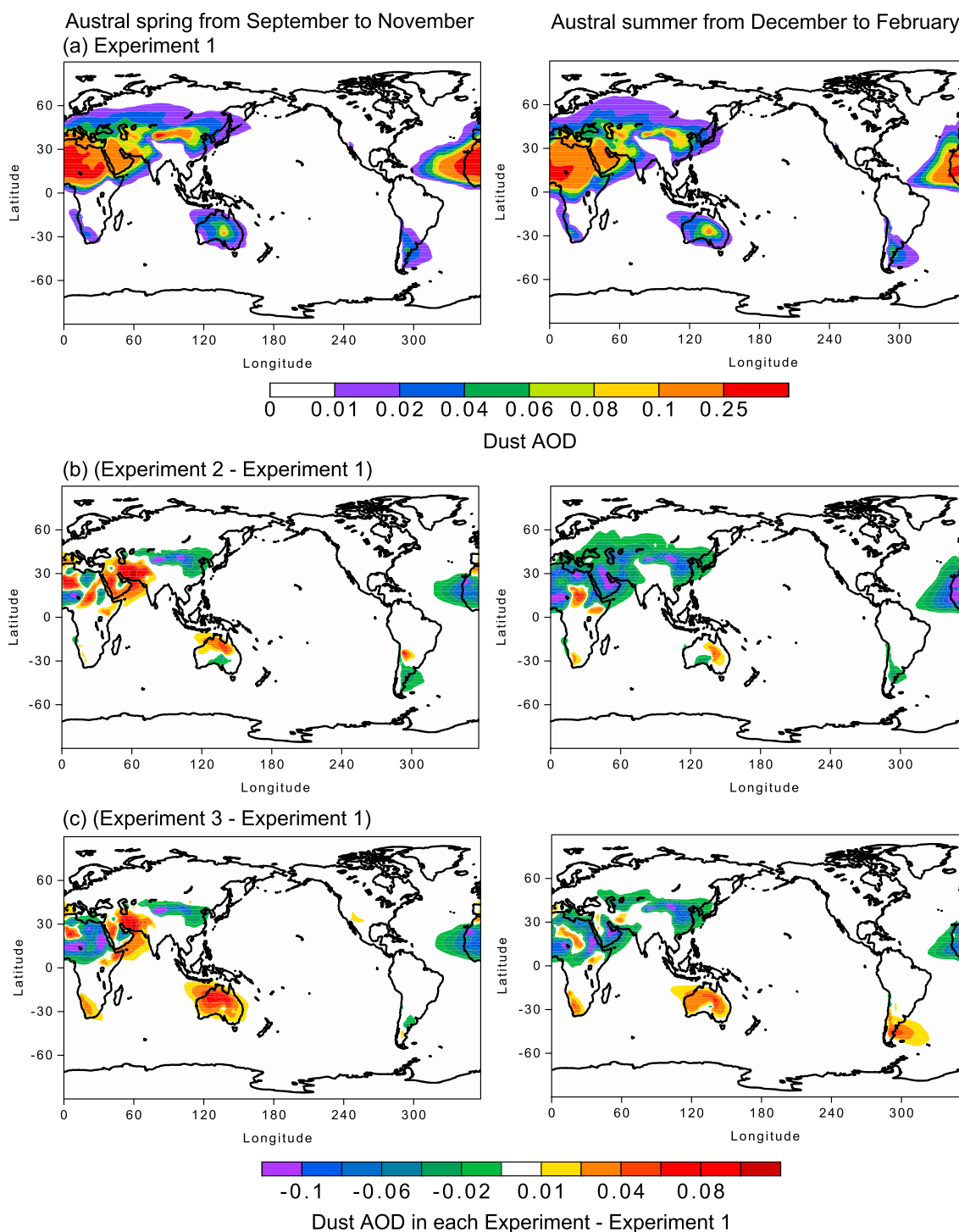
Figure 1. Global distribution of the dust AOD during austral spring from September to November and during austral summer from December to February. Results are shown for the model simulations from (a) Experiment 1 and the differences from Experiment 1 to (b) Experiment 2 and (c) Experiment 3.

Experiment 5 similarly accounts for the suppression of dust emissions due to vegetated areas in barren and open shrublands but instead uses the data set of *Li et al.* [2013] to parameterize suppressing effects of vegetation cover on dust emissions. Specifically, we fit an exponential function to the data set (Figure S2b):

$$F_{bare} = C_c \times \exp(-C_d \times f_{bare}) \times f_{land}, \left(R^2 = 0.33 \right), \quad (17)$$

where $C_c = 0.0292$ and $C_d = 3.5$. The two different simulations for Experiment 3 and Experiment 5 are intended
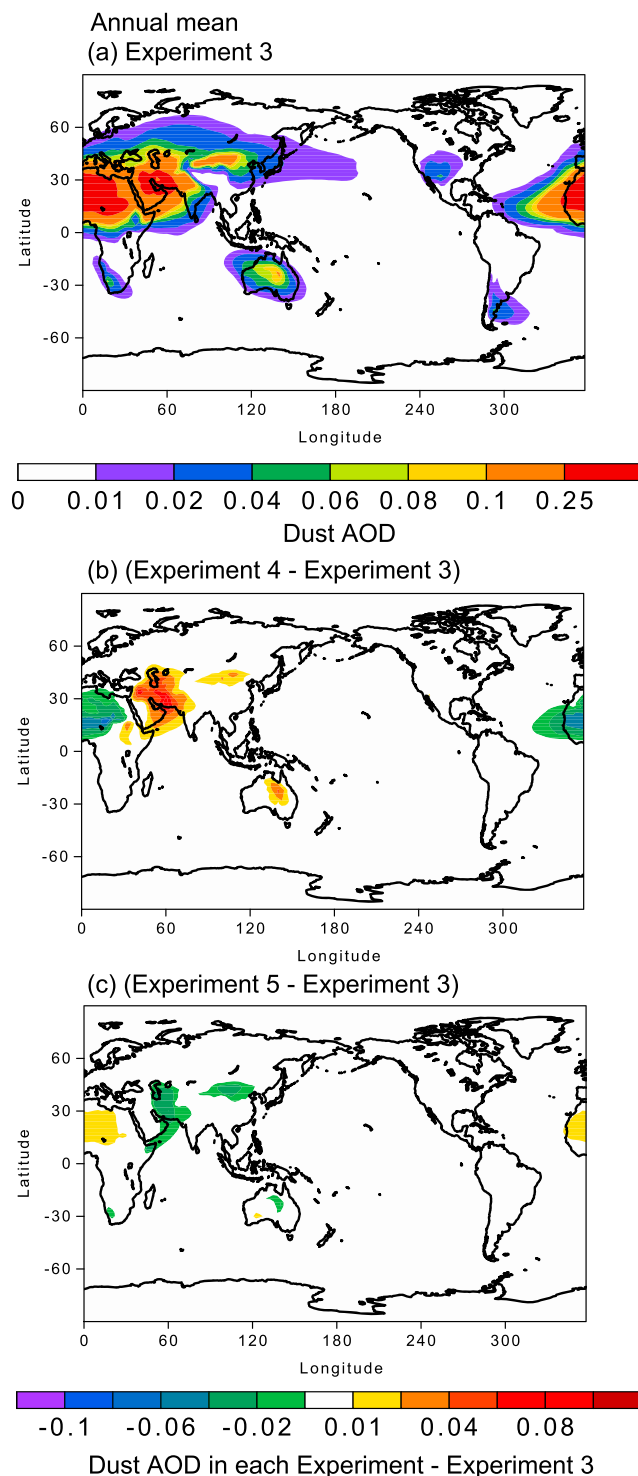
Figure 2. Global distribution of the annually averaged dust AOD. Results are shown for the model simulations from (a) Experiment 3 and the differences from Experiment 3 to (b) Experiment 4 and (c) Experiment 5.

to capture the uncertainties associated with the formulas which represent suppressing effects of vegetation cover on dust emissions. In this way, the heterogeneity of the surface features is accounted for at finer resolution than the model grid, although the dust emission at subgrid scale is not explicitly and spatially represented. Here tagged-tracer simulations were conducted with the dust emissions from barren lands only and those from open shrublands only.

2.6. Observations of Aerosol Optical Properties

We adjusted the global scaling constant for each dust emission scheme in order to maximize agreement with Aerosol Robotic Network (AERONET) AOD measurements near the dust source regions, similar to that was done in *Kok et al.* [2014b] (Figure S3). The AOD and single-scattering albedo at 440, 500, 550, and 675 nm were calculated online, following *Xu and Penner* [2012]. We compare the model results against satellite measurements of AOD averaged for "dust-dominated days" (Collection 6 MODIS DB). These are defined by three criteria, which were based on physical and optical properties of aerosols, after *Ginoux et al.* [2012]:

1. Ångström exponent between 440 and 500 nm (412 and 470 nm) is smaller than 1.
2. Single-scattering albedo at 440 nm (412 nm) is less than 0.95.
3. Difference of the single-scattering albedo between 440 and 675 nm (412 and 670 nm) is larger than 1.

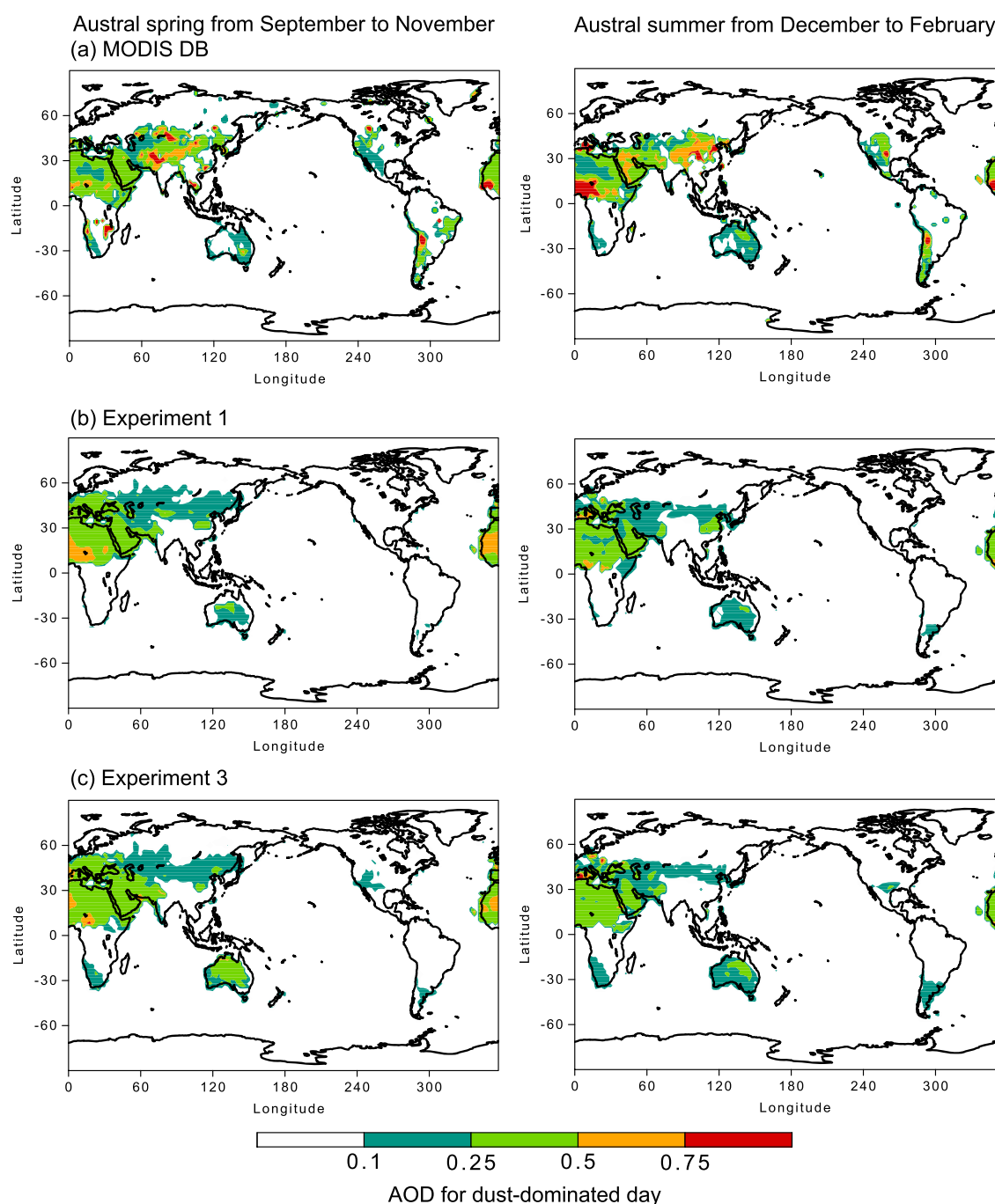We also compare the percentage of days that were classified as dust-dominated days in each season per total dust-dominated days in the year of 2004 between the model results and satellite measurements. For this comparison, we used the data for which the MODIS BD retrieval per $0.1° \times 0.1°$ grid cell exists.

Austral spring from September to November
(a) MODIS DB

Austral summer from December to February

(b) Experiment 1

(c) Experiment 3

AOD for dust-dominated day

Figure 3. Global distributions of AOD averaged for dust-dominated days during austral spring from September to November and during austral summer from December to February. Results are shown for (a) Collection 6 MODIS DB, (b) Experiment 1, and (c) Experiment 3.

3. Results and Discussions

3.1. Mineral Dust Emission and Aerosol Optical depth

3.1.1. Effect of Soil Moisture on Dust Emission

The dust sources of Fe in the SH are highly sensitive to the emission schemes and soil moisture, in contrast to the global emissions (Table 2 and Figure S4). In particular, the use of satellite measurements of soil moisture in the dust emission scheme results in an increase in emissions from sparsely vegetated regions in the SH, approximately doubling the Fe emissions from 7 to 8 Tg yr^{-1} in Experiments 1 and 2 to 12–15 Tg yr^{-1} in
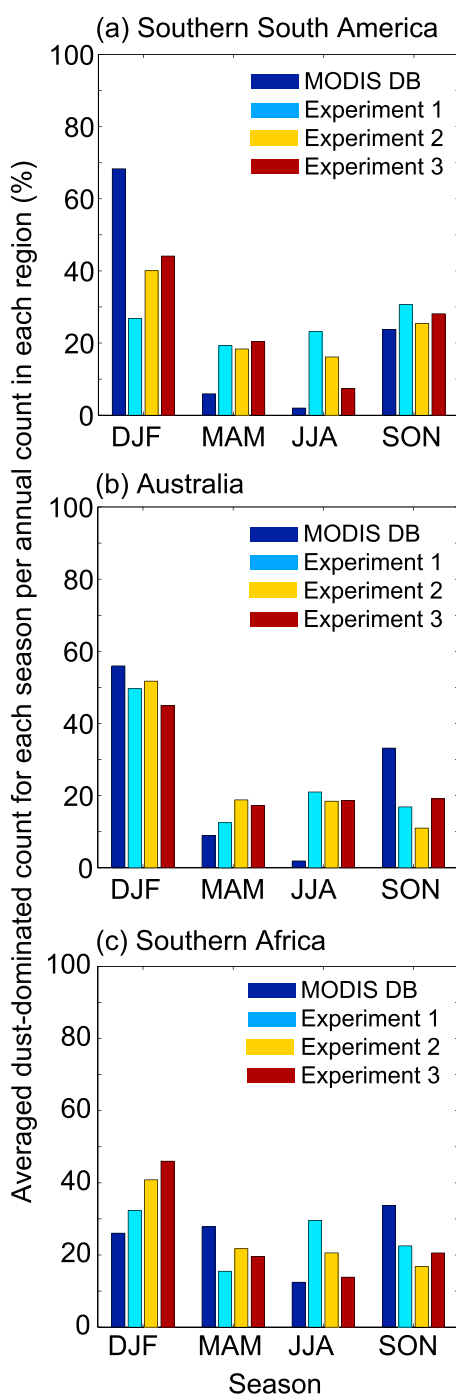
Figure 4. Seasonal changes in dust-dominated count summed for each season (December–February, March–May, June–August, and September–November) per that for annual count in each region (%). Results are presented for (a) southern South America (40–60°S. 280–305°E), (b) Australia (20–36°S, 115–150°E), and (c) southern Africa (22–40°S, 10–25°E). Results are shown for Collection 6 MODIS DB, Experiment 1, Experiment 2, and Experiment 3.

Experiments 3–5. Global distributions of threshold friction velocity for Experiments 2 and 3 showed substantial sensitivity to soil moisture, compared to that of threshold wind velocity for Experiment 1 (Figure S5). The dust emissions for Experiment 2 are more often suppressed due to wetter conditions, especially in the SH, in case the bias in modeled soil moisture content was not corrected (Table 2 and Figure 1).

3.1.2. Effect of Soil Texture on Dust Emission

In Experiment 4, the low clay content in soils is expressed in low values of the parameter γ, which represents the capability of the soil to emit dust aerosols through saltation processes (Figure S6). This capacity for Experiment 3 is higher than Experiment 4 around low clay content (i.e., low values of the parameter γ in Experiment 4), especially in the southern Sahara. Thus, dust AOD over a large fraction of North Africa in Experiment 3 is higher than that in Experiment 4 (Figure 2). This is qualitatively consistent with the observation that almost half of North African dust storms originate from areas with sand dunes (i.e., low clay content) [*Crouvi et al.*, 2012]. On the other hand, the capacity for Experiment 3 is lower than Experiment 4 around relatively high clay content (>0.2) over the Middle East, such as Iran and Iraq. Thus, dust AOD in Experiment 3 is lower than that in Experiment 4 over the Middle East where modeled AOD was considerably overestimated against the AERONET measurements (Figure S3).

3.1.3. Effect of Surface Vegetation Cover on Dust Emission

The values of the bare ground cover (F_{bare}), which represents the susceptibility of areas to wind erosion, are larger for both cases over areas with low vegetation and snow cover (Figure S7). Although the dust AOD in the SH is substantially lower than that in the NH, many new dust source regions appear with the introduction of dust emissions from sparsely vegetated surfaces (Figures 1 and 2). The most intense sources are located in Australia and southern Africa, in addition to larger dust emissions from Patagonia in austral summer.

Table 3. Atmospheric Deposition of Fe From Dust (Tg Fe) During Austral Spring and Summer Into the Southern Ocean (>45°S) From Five Simulations[a]

Simulation	Spring	Summer	Annual
Experiment 1	0.29	0.30	1.0
Experiment 2	0.09 (79%)	0.21 (96%)	0.46 (87%)
Experiment 3	0.37 (95%)	0.73 (98%)	1.5 (96%)
Experiment 4	0.42 (95%)	0.83 (98%)	1.7 (96%)
Experiment 5	0.35 (97%)	0.65 (98%)	1.4 (97%)

[a]The numbers in parentheses represent the fractional contribution (percentage) of open shrublands to the sum of deposition from barren soil and open shrublands.

3.1.4. Comparison of Aerosol Optical Properties With Observations

The changes in simulated SH source strengths are difficult to verify, mostly because the numbers of dusty days from both the model results and observations are quite low in the SH [*Ginoux et al.*, 2012; *Ridley et al.*, 2016]. Nonetheless, the seasonal changes of AOD averaged for dust-dominated days with our improved dust emission module are generally consistent with satellite imagery over the source regions (Figure 3). In
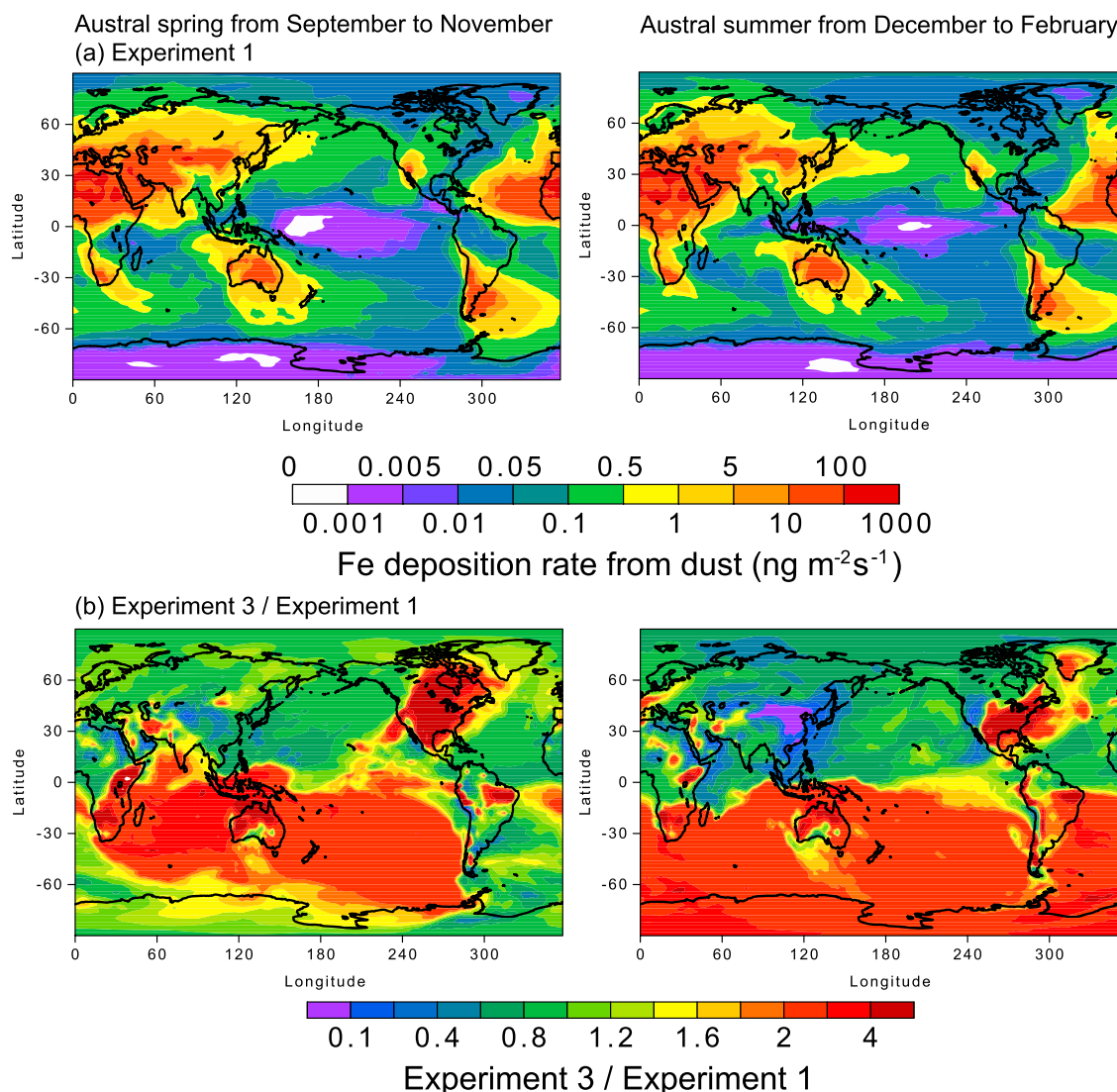

Figure 5. Atmospheric Fe deposition from dust sources during austral spring from September to November and during austral summer from December to February. Results are shown for (a) Experiment 1 and (b) the ratios from Experiment 1 to Experiment 3.
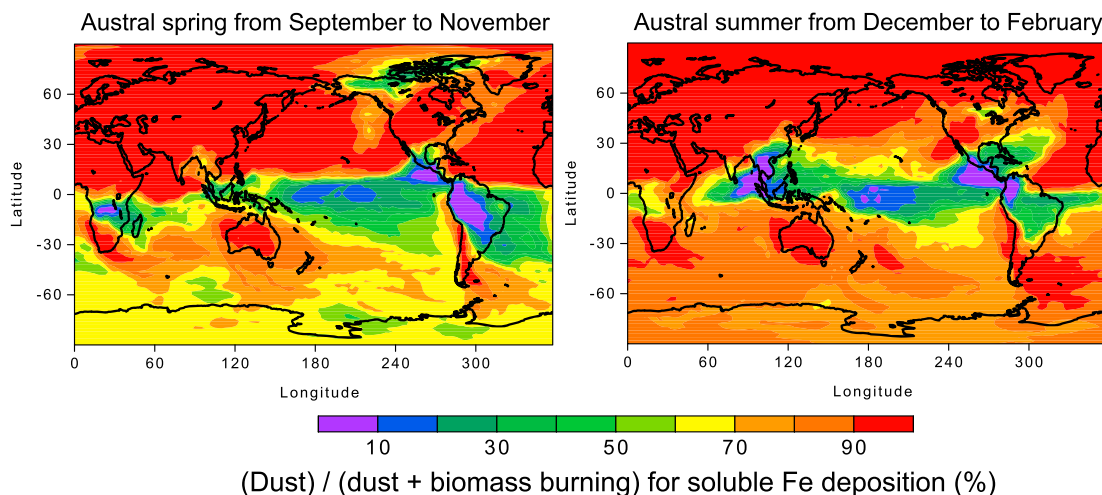
Figure 6. Contribution of soluble Fe deposition from dust sources to the sum of soluble Fe deposition from dust and biomass burning sources during austral spring from September to November and during austral summer from December to February. Results are shown for Experiment 3.

southern South America and Australia, both our improved model from Experiment 3 and MODIS DB showed the maximum number of dust-dominated days in summer (Figure 4). In southern Africa, our improved model (Experiment 3) reproduced the significant source areas over the Kalahari Desert and near ephemeral lakes in Bushmanland, in contrast to the conventional dust emission scheme (Experiment 1).

3.2. Atmospheric Fe Input From Dust Source Regions to Southern Ocean

We used our improved dust emission module to more accurately simulate the deposition of Fe from dust ($Tg\,Fe\,yr^{-1}$) into the Southern Ocean (Table 3). The estimates of Fe deposition significantly increase from $0.46\,Tg\,yr^{-1}$ in the simulations with no bias correction in modeled soil moisture (Experiment 2) to $1.4–1.7\,Tg\,yr^{-1}$ with the bias correction (Experiments 3–5). Possible underestimate of active dust sources in Patagonia was reported in a climate model even after specific scale factor was used to match the observation of dust deposition within an order of magnitude [*Albani et al.*, 2016]. Our estimate of Fe deposition to the Southern Ocean lies within their uncertainty range. However, the dust emissions with our improved method
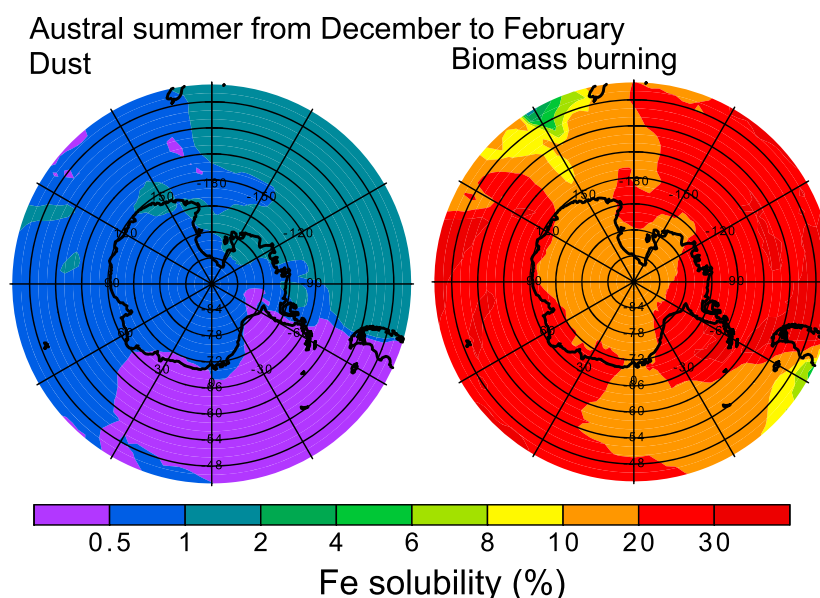

Figure 7. Fractional Fe solubility deposited from dust and biomass burning sources to the Southern Ocean (>45°S) and Antarctica during austral summer from December to February. Results are shown for Experiment 3.
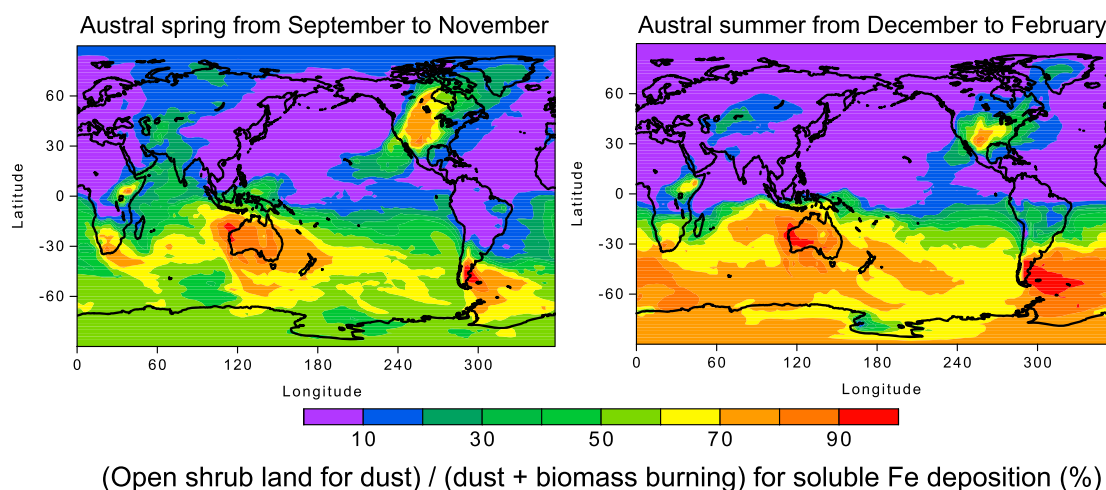
Figure 8. Contribution of soluble Fe deposition from open shrublands for dust to the sum of soluble Fe deposition from dust and biomass burning sources during austral spring from September to November and during austral summer from December to February. Results are shown for Experiment 3.

are considerably larger than their estimate (0.56 Tg yr^{-1}) and thus may contribute to the reduction of the underestimate.

Our model results nonetheless show similar transport pathways from southern South America (Argentina and Chile), Australia, and southern Africa (Namibia and South Africa) to the Southern Ocean (Figure 5a). Our improved model results indicate significantly larger Fe input from the dust sources, especially Patagonian dust, to the Southern Ocean in summer by more than a factor of 2, compared to the conventional dust emission scheme (Figure 5b). Consequently, the dust is the major source of atmospheric soluble Fe to the Southern Ocean in summer, which is consistent with the seasonality measured in Antarctica [*Winton et al.,* 2016] (Figure 6).

Our model estimated lower Fe solubility deposited to the Southern Ocean from dust (<2%) than that from biomass burning aerosols (>10%), because of slower Fe dissolution for dust aerosols (Figure 7). This is also consistent with the observed background fractional Fe solubility of ~0.7% from mineral dust sources [*Winton et al.,* 2016]. In contrast, high Fe solubility (18%) is observed for aerosols influenced by fires over the Southern Ocean [*Bowie et al.,* 2009]. Therefore, the Fe-containing aerosols affected by fires may be associated with sporadic high Fe solubility, which was measured in Antarctica [*Conway et al.,* 2015; *Winton et al.,* 2016]. Further investigation of the processes of enhanced Fe solubility over the Southern Ocean is needed to improve our understanding of bioavailable Fe supply from sparsely vegetated regions to the oceans and their effects on the marine ecosystems.

We compare soluble Fe deposition from open shrublands to the sum of soluble Fe deposition from dust and biomass burning sources during austral spring from September to November and during austral summer from December to February (Figure 8). Remarkably, the contribution of soluble Fe deposition downwind from open shrublands in the SH exceeds more than 80% in austral summer. The contribution of soluble Fe from open shrublands to the South Indian, South Pacific, and South Atlantic increases from spring to summer. Our estimate of soluble Fe deposition to the Southern Ocean in summer is approximately doubled from 1.2 Gg yr^{-1} (Experiment 1) to 2.3 Gg yr^{-1} (Experiments 3), due to improved dust emission module. Our model results indicate that dust emission from open shrublands contributes to 83% of total soluble Fe deposition into the Southern Ocean during summer. The larger seasonality of atmospheric soluble Fe input has important implications for primary marine productivity in the HNLC regions of the Southern Ocean.

4. Conclusions

Accurate estimates of seasonal dust emissions in the SH is key to constraining bioavailable Fe deposition to the Southern Ocean, which in turn is critical in understanding the role of marine ecosystems on carbon cycle and climate. In this study, we tested the hypothesis that sparsely vegetated surfaces in arid and semiarid

regions are important sources of Fe-containing aerosols to the Southern Ocean. We used the physically based dust emission parameterization of *Kok et al.* [2014a], which is more sensitive to soil moisture than the conventional scheme of *Ginoux et al.* [2001]. Since further advances in the treatments of soil moisture and associated land surface properties are required in reanalysis data of meteorological fields [e.g., *De Lannoy et al.*, 2014], the hypothesis is difficult to test with current global transport models. We therefore enhanced the fidelity of the dust emission scheme using satellite retrievals of soil moisture and surface vegetation cover. Subsequently, we examined the sensitivities of dust emissions to different treatments of soil moisture, soil texture, and vegetation cover in the atmospheric chemistry transport model. We then evaluated the simulated aerosol optical properties for the dust-dominated days using satellite measurements (MODIS BD).

Our improved model showed more than twofold increases in dust Fe input to the Southern Ocean in summer, especially from Patagonian dust, compared to results with the conventional dust emission scheme. Tagged-tracer experiments indicated that open shrublands mainly contributed to dust Fe input into the Southern Ocean during austral summer and that their contribution accounted for 97% of total Fe deposition from dust and biomass burning sources. These results support the hypothesis that much of the Fe input to the Southern Ocean is due to dust originating from sparsely vegetated regions. As such, our results highlight the need for improving the process-based understanding of the dependence of dust emission on soil moisture and vegetation. This is especially crucial to assess future impacts of climate and land use changes on dust emissions in the Southern Hemisphere and their environmental consequences.

References

Albani, S., et al. (2016), Paleodust variability since the Last Glacial Maximum and implications for iron inputs to the ocean, *Geophys. Res. Lett.*, *43*, 3944–3954, doi:10.1002/2016GL067911.

Bhattachan, A., and P. D'Odorico (2014), Can land use intensification in the Mallee, Australia increase the supply of soluble iron to the Southern Ocean?, *Sci. Rep.*, *4*, doi:10.1038/srep06009.

Bhattachan, A., P. D'Odorico, M. C. Baddock, T. M. Zobeck, G. S. Okin, and N. Cassar (2012), The Southern Kalahari: A potential new dust source in the Southern Hemisphere?, *Environ. Res. Lett.*, *7*, doi:10.1088/1748-9326/7/2/024001.

Bowie, A. R., D. Lannuzel, T. A. Remenyi, T. Wagener, P. J. Lam, P. W. Boyd, C. Guieu, A. T. Townsend, and T. W. Trull (2009), Biogeochemical iron budgets of the Southern Ocean south of Australia: Decoupling of iron and nutrient cycles in the subantarctic zone by the summertime supply, *Global Biogeochem. Cycles*, *23*, GB4034, doi:10.1029/2009GB003500.

Boyd, P. W., D. S. Mackie, and K. A. Hunter (2010), Aerosol iron deposition to the surface ocean—Modes of iron supply and biological responses, *Mar. Chem.*, *120*, 128–143, doi:10.1016/j.marchem.2009.01.008.

Bullard, J., M. Baddock, G. McTainsh, and J. Leys (2008), Sub-basin scale dust source geomorphology detected using MODIS, *Geophys. Res. Lett.*, *35*, L15404, doi:10.1029/2008GL033928.

Chappell, A., S. Van Pelt, T. Zobeck, and Z. Dong (2010), Estimating aerodynamic resistance of rough surfaces using angular reflectance, *Remote Sens. Environ.*, *114*(7), 1462–1470, doi:10.1016/j.rse.2010.01.025.

Chen, H., and V. H. Grassian (2013), Iron dissolution of dust source materials during simulated acidic processing: The effect of sulfuric, acetic, and oxalic acids, *Environ. Sci. Technol.*, *47*, 10,312–10,321, doi:10.1021/es401285s.

Conway, T., E. Wolff, R. Röthlisberger, R. Mulvaney, and H. Elderfield (2015), Constraints on soluble aerosol iron flux to the Southern Ocean at the Last Glacial Maximum, *Nat. Commun.*, *6*, 7850, doi:10.1038/ncomms8850.

Crouvi, O., K. Schepanski, R. Amit, A. R. Gillespie, and Y. Enzel (2012), Multiple dust sources in the Sahara desert: The importance of sand dunes, *Geophys. Res. Lett.*, *39*, L13401, doi:10.1029/2012GL052145.

De Lannoy, G. J. M., R. D. Koster, R. H. Reichle, S. P. P. Mahanama, and Q. Liu (2014), An updated treatment of soil texture and associated hydraulic properties in a global land modeling system, *J. Adv. Model. Earth Syst.*, *6*, 957–979, doi:10.1002/2014MS000330.

DiMiceli, C. M., M. L. Carroll, R. A. Sohlberg, C. Huang, M. C. Hansen, and J. R. G. Townshend (2011), *Annual Global Automated MODIS Vegetation Continuous Fields (MOD44B) at 250 m Spatial Resolution for Data Years Beginning Day 65, 2000–2010, Collection 5 Percent Tree Cover*, Univ. of Maryland, College Park, Fairlie, New Zealand.

D'Odorico, P., A. Bhattachan, K. F. Davis, S. Ravi, and C. W. Runyan (2013), Global desertification: Drivers and feedbacks, *Adv. Water Res.*, *51*, 326–344, doi:10.1016/j.advwatres.2012.01.013.

Fairlie, T. D., D. J. Jacob, J. E. Dibb, B. Alexander, M. A. Avery, A. van Donkelaar, and L. Zhang (2010), Impact of mineral dust on nitrate, sulfate, and ozone in transpacific Asian pollution plumes, *Atmos. Chem. Phys.*, *10*, 3999–4012, doi:10.5194/acp-10-3999-2010.

Fécan, F., B. Marticorena, and G. Bergametti (1999), Parametrization of the increase of the aeolian erosion threshold wind friction velocity due to soil moisture for arid and semi-arid areas, *Ann. Geophys.*, *17*, 149–157, doi:10.1007/s00585-999-0149-7.

Feng, Y., and J. E. Penner (2007), Global modeling of nitrate and ammonium: Interaction of aerosols and tropospheric chemistry, *J. Geophys. Res.*, *112*, D01304, doi:10.1029/2005JD006404.

Friedl, M. A., D. Sulla-Menashe, B. Tan, A. Schneider, N. Ramankutty, A. Sibley, and X. Huang (2010), MODIS collection 5 global land cover: Algorithm refinements and characterization of new datasets, *Remote Sens. Environ.*, *114*, 168–182.

Fryrear, D. W. (1985), Soil cover and wind erosion, *Trans. ASAE*, *28*(3), 781–784, doi:10.13031/2013.32337.

Gherboudj, I., S. N. Beegum, B. Marticorena, and H. Ghedira (2015), Dust emission parameterization scheme over the MENA region: Sensitivity analysis to soil moisture and soil texture, *J. Geophys. Res. Atmos.*, *120*, 10,915–10,938, doi:10.1002/2015JD023338.

Gillette, D. A. (1977), Fine particulate emissions due to wind erosion, *Trans. ASAE*, *20*, 890–897.

Ginoux, P., M. Chin, I. Tegen, J. M. Prospero, B. Holben, O. Dubovik, and S.-J. Lin (2001), Sources and distributions of dust aerosols simulated with the GOCART model, *J. Geophys. Res.*, *106*, 20,255–20,274, doi:10.1029/2000JD000053.

Ginoux, P., J. M. Prospero, T. E. Gill, N. C. Hsu, and M. Zhao (2012), Global-scale attribution of anthropogenic and natural dust sources and their emission rates based on MODIS Deep Blue aerosol products, *Rev. Geophys.*, *50*, RG3005, doi:10.1029/2012RG000388.

Guenther, A. B., X. Jiang, C. L. Heald, T. Sakulyanontvittaya, T. Duhl, L. K. Emmons, and X. Wang (2012), The Model of Emissions of Gases and Aerosols from Nature version 2.1 (MEGAN2.1): An extended and updated framework for modeling biogenic emissions, *Geosci. Model Dev.*, *5*, 1471–1492, doi:10.5194/gmd-5-1471-2012.

Hajima, T., M. Kawamiya, M. Watanabe, E. Kato, K. Tachiiri, M. Sugiyama, S. Watanabe, H. Okajima, and A. Ito (2014), Modeling in Earth system science up to and beyond IPCC AR5, *Progr. Earth Planet. Sci.*, *1*, 1–25, doi:10.1186/s40645-014-0029-y.

Haustein, K., R. Washington, J. King, G. Wiggs, D. S. G. Thomas, F. D. Eckardt, R. G. Bryant, and L. Menut (2015), Testing the performance of state-of-the-art dust emission schemes using DO4Models field data, *Geosci. Model Dev.*, *8*, 341–362, doi:10.5194/gmd-8-341-2015.

Ishizuka, M., M. Mikami, J. Leys, Y. Yamada, S. Heidenreich, Y. Shao, and G. H. McTainsh (2008), Effects of soil moisture and dried raindroplet crust on saltation and dust emission, *J. Geophys. Res.*, *113*, D24212, doi:10.1029/2008JD009955.

Ito, A. (2011), Mega fire emissions in Siberia: Potential supply of bioavailable iron from forests to the ocean, *Biogeosciences*, *8*, 1679–1697.

Ito, A. (2012), Contrasting the effect of iron mobilization on soluble iron deposition to the ocean in the Northern and Southern Hemispheres, *J. Meteorol. Soc. Jpn.*, *90A*, 167–188, doi:10.2151/jmsj.2012-A09.

Ito, A. (2013), Global modeling study of potentially bioavailable iron input from shipboard aerosol sources to the ocean, *Global Biogeochem. Cycles*, *27*, 1–10, doi:10.1029/2012GB004378.

Ito, A. (2015), Atmospheric processing of combustion aerosols as a source of bioavailable iron, *Environ. Sci. Technol. Lett.*, *2*(3), 70–75, doi:10.1021/acs.estlett.5b00007.

Ito, A., and J. E. Penner (2004), Global estimates of biomass burning emissions based on satellite imagery for the year 2000, *J. Geophys. Res.*, *109*, D14S05, doi:10.1029/2003JD004423.

Ito, A., and L. Xu (2014), Response of acid mobilization of iron-containing mineral dust to improvement of air quality projected in the future, *Atmos. Chem. Phys.*, *14*, 3441–3459, doi:10.5194/acp-14-3441-2014.

Ito, A., and Y. Feng (2010), Role of dust alkalinity in acid mobilization of iron, *Atmos. Chem. Phys.*, *10*, 9237–9250.

Ito, A., and Z. Shi (2016), Delivery of anthropogenic bioavailable iron from mineral dust and combustion aerosols to the ocean, *Atmos. Chem. Phys.*, *16*, 85–99, doi:10.5194/acp-16-85-2016.

Ito, A., S. Sillman, and J. E. Penner (2007), Effects of additional nonmethane volatile organic compounds, organic nitrates, and direct emissions of oxygenated organic species on global tropospheric chemistry, *J. Geophys. Res.*, *112*, D06309, doi:10.1029/2005JD006556.

Ito, A., S. Sillman, and J. E. Penner (2009), Global chemical transport model study of ozone response to changes in chemical kinetics and biogenic volatile organic compounds emissions due to increasing temperatures: Sensitivities to isoprene nitrate chemistry and grid resolution, *J. Geophys. Res.*, *114*, D09301, doi:10.1029/2008JD011254.

Ito, A., J. F. Kok, Y. Feng, and J. E. Penner (2012), Does a theoretical estimation of the dust size distribution at emission suggest more bioavailable iron deposition? *Geophys. Res. Lett.*, *39*, L05807, doi:10.1029/2011GL050455.

Ito, A., G. Lin, and J. E. Penner (2014), Reconciling modeled and observed atmospheric deposition of soluble organic nitrogen at coastal locations, *Global Biogeochem. Cycles*, *28*, 617–630, doi:10.1002/2013GB004721.

Ito, A., G. Lin, and J. E. Penner (2015), Global modeling study of soluble organic nitrogen from open biomass burning, *Atmos. Environ.*, *121*, 103–112, doi:10.1016/j.atmosenv.2015.01.031.

Jickells, T., and C. M. Moore (2015), The importance of atmospheric deposition for ocean productivity, *Annu. Rev. Ecol. Evol. Syst.*, *46*(1), 481–501.

Johnson, M. S., N. Meskhidze, F. Solmon, S. Gasso, P. Y. Chuang, D. M. Gaiero, R. M. Yantosca, S. L. Wu, Y. X. Wang, and C. Carouge (2010), Modeling dust and soluble iron deposition to the South Atlantic Ocean, *J. Geophys. Res.*, *115*, D15202, doi:10.1029/2009JD013311.

Journet, E., Y. Balkanski, and S. P. Harrison (2014), A new data set of soil mineralogy for dust-cycle modeling, *Atmos. Chem. Phys.*, *14*(8), 3801–3816, doi:10.5194/acp-14-3801-2014.

Kavouras, I. G., G. Nikolich, V. Etyemezian, D. W. DuBois, J. King, and D. Shafer (2012), In situ observations of soil minerals and organic matter in the early phases of prescribed fires, *J. Geophys. Res.*, *117*, D12313, doi:10.1029/2011JD017420.

Kok, J. F. (2011), A scaling theory for the size distribution of emitted dust aerosols suggests climate models underestimate the size of the global dust cycle, *Proc. Natl. Acad. Sci. U.S.A.*, *108*(3), 1016–1021.

Kok, J. F., E. J. R. Parteli, T. I. Michaels, and D. B. Karam (2012), The physics of wind-blown sand and dust, *Rep. Prog. Phys.*, *75*, 106901, doi:10.1088/0034-4885/75/10/106901.

Kok, J. F., et al. (2014a), An improved dust emission model—Part 1: Model description and comparison against measurements, *Atmos. Chem. Phys.*, *14*, 13,023–13,041, doi:10.5194/acp-14-13023-2014.

Kok, J. F., S. Albani, N. M. Mahowald, and D. S. Ward (2014b), An improved dust emission model—Part 2: Evaluation in the Community Earth System Model, with implications for the use of dust source functions, *Atmos. Chem. Phys.*, *14*, 13,043–13,061, doi:10.5194/acp-14-13043-2014.

Li, F., P. Ginoux, and V. Ramaswamy (2008), Distribution, transport, and deposition of mineral dust in the Southern Ocean and Antarctica: Contribution of major sources, *J. Geophys. Res.*, *113*, D10207, doi:10.1029/2007JD009190.

Li, J., G. S. Okin, J. E. Herrick, J. Belnap, M. E. Miller, K. Vest, and A. E. Draut (2013), Evaluation of a new model of aeolian transport in the presence of vegetation, *J. Geophys. Res. Earth Surf.*, *118*, 288–306, doi:10.1002/jgrf.20040.

Lin, G., S. Sillman, J. E. Penner, and A. Ito (2014), Global modeling of SOA: the use of different mechanisms for aqueous-phase formation, *Atmos. Chem. Phys.*, *14*, 5451–5475, doi:10.5194/acp-14-5451-2014.

Liu, X., J. E. Penner, and M. Herzog (2005), Global modeling of aerosol dynamics: Model description, evaluation and interactions between sulfate and non-sulfate aerosols, *J. Geophys. Res.*, *110*, D18206, doi:10.1029/2004JD005674.

Mackie, D. S., P. W. Boyd, K. A. Hunter, and G. H. McTainsh (2005), Simulating the cloud processing of iron in Australian dust: pH and dust concentration, *Geophys. Res. Lett.*, *32*, L06809, doi:10.1029/2004GL022122.

Mahowald, N. (2007), Anthropocene changes in desert area: Sensitivity to climate model predictions, *Geophys. Res. Lett.*, *34*, L18817, doi:10.1029/2007GL030472.

Mahowald, N. M., and J.-L. Dufresne (2004), Sensitivity of TOMS aerosol index to boundary layer height: Implications for detection of mineral aerosol sources, *Geophys. Res. Lett.*, *31*, L03103, doi:10.1029/2003GL018865.

Marticorena, B., and G. Bergametti (1995), Modeling the atmospheric dust cycle: 1. Design of a soil derived dust production scheme, *J. Geophys. Res.*, *100*, 16,415–16,430, doi:10.1029/95JD00690.

Martin, J. H., R. M. Gordon, and S. E. Fitzwater (1990), Iron in Antarctic waters, *Nature*, *345*, 156–158.

McConnell, J. R., A. J. Aristarain, J. R. Banta, P. R. Edwards, and J. C. Simoes (2007), 20th-century doubling in dust archived in an Antarctic Peninsula ice core parallels climate change and desertification in South America, *Proc. Natl. Acad. Sci. U.S.A.*, *104*, 5743–5748.

Mikami, M., Y. Yamada, M. Ishizuka, T. Ishimaru, W. Gao, and F. Zeng (2005), Measurement of saltation process over Gobi and sand dunes in the Taklimakan desert, China, with newly developed sand particle counter, *J. Geophys. Res.*, *110*, D18S02, doi:10.1029/2004JD004688.

Myneni, R., Y. Knyazikhin, T. Park. (2015), MCD15A2H MODIS/Terra + Aqua leaf area index/FPAR 8-day L4 Global 500 m SIN Grid V006, NASA EOSDIS Land Processes DAAC. [Available at http://doi.org/10.5067/MODIS/MCD15A2H.006.]

Nickovic, S., A. Vukovic, M. Vujadinovic, V. Djurdjevic, and G. Pejanovic (2012), Technical Note: High-resolution mineralogical database of dust-productive soils for atmospheric dust modeling, *Atmos. Chem. Phys.*, *12*, 845–855.

Okin, G. S. (2008), A new model of wind erosion in the presence of vegetation, *J. Geophys.*, *113*, F02S10, doi:10.1029/2007JF000758.

Okin, G. S., and D. A. Gillette (2001), Distribution of vegetation in wind-dominated landscapes: Implications for wind erosion modeling and landscape processes, *J. Geophys. Res.*, *106*, 9673–9683, doi:10.1029/2001JD900052.

Owe, M., R. de Jeu, and T. Holmes (2008), Multisensor historical climatology of satellite-derived global land surface moisture, *J. Geophys. Res.*, *113*, F01002, doi:10.1029/2007JF000769.

Palmer, P. I., et al. (2006), Quantifying the seasonal and interannual variability of North American isoprene emissions using satellite observations of the formaldehyde column, *J. Geophys. Res.*, *111*, D12315, doi:10.1029/2005JD006689.

Prospero, J. M., P. Ginoux, O. Torres, S. E. Nicholson, and T. E. Gill (2002), Environmental characterization of global sources of atmospheric soil dust identified with the Nimbus 7 Total Ozone Mapping Spectrometer (TOMS) absorbing aerosol product, *Rev. Geophys.*, *40*(1), 1002, doi:10.1029/2000RG000095.

Ravi, S., M. C. Baddock, T. M. Zobeck, and J. Hartman (2012), Field evidence for differences in post-fire sediment transport related to vegetation type in semi-arid rangelands, *Aeolian Res.*, *7*, 3–10, doi:10.1016/j.aeolia.2011.12.002.

Ridley, D. A., C. L. Heald, J. F. Kok, and C. Zhao (2016), An observationally constrained estimate of global dust aerosol optical depth, *Atmos. Chem. Phys.*, *16*, 15,097–15,117, doi:10.5194/acp-16-15097-2016.

Rotman, D. A., et al. (2004), IMPACT, the LLNL 3-D global atmospheric chemical transport model for the combined troposphere and stratosphere: Model description and analysis of ozone and other trace gases, *J. Geophys. Res.*, *109*, D04303, doi:10.1029/2002JD003155.

Schepanski, K., I. Tegen, M. C. Todd, B. Heinold, G. Bönisch, B. Laurent, and A. Macke (2009), Meteorological processes forcing Saharan dust emission inferred from MSG-SEVIRI observations of subdaily dust source activation and numerical models, *J. Geophys. Res.*, *114*, D10201, doi:10.1029/2008JD010325.

Schulz, M., et al. (2012), Atmospheric transport and deposition of mineral dust to the ocean: Implications for research needs, *Environ. Sci. Technol.*, *46*(19), 10,390–10,404.

Shao, Y. (2008), *Physics and Modelling of Wind Erosion*, *Atmos. Oceanogr. Sci. Libr.*, vol. 37, Kluwer Acad., Dordrecht, Netherlands.

Shao, Y., K. H. Wyrwoll, A. Chappell, J. Huang, Z. Lin, G. H. McTainsh, M. Mikami, T. Y. Tanaka, X. Wang, and S. Yoon (2011), Dust cycle: An emerging core theme in Earth system science, *Aeolian Res.*, *2*(4), 181–204.

Stillman, S., X. Zeng, and M. G. Bosilovich (2016), Evaluation of 22 precipitation and 23 soil moisture products over a semiarid area in southeastern Arizona, *J. Hydrometeorol.*, *17*(1), 211–230.

Sweeney, M. R., and J. A. Mason (2013), Mechanisms of dust emission from Pleistocene loess deposits, Nebraska, USA, *J. Geophys. Res. Earth Surf.*, *118*, 1460–1471, doi:10.1002/jgrf.20101.

Vest, K. R., A. J. Elmore, J. M. Kaste, G. S. Okin, and J. Li (2013), Estimating total horizontal aeolian flux within shrub-invaded groundwater-dependent meadows using empirical and mechanistic models, *J. Geophys. Res. Earth Surf.*, *118*, 1132–1146, doi:10.1002/jgrf.20048.

Wang, Q., et al. (2011), Sources of carbonaceous aerosols and deposited black carbon in the Arctic in winter-spring: Implications for radiative forcing, *Atmos. Chem. Phys.*, *11*(23), 12,453–12,473, doi:10.5194/acp-11-12453-2011.

Wang, X., L. Zhang, and M. D. Moran (2014), Bulk or modal parameterizations for below-cloud scavenging of fine, coarse, and giant particles by both rain and snow, *J. Adv. Model. Earth Syst.*, *6*, 1301–1310, doi:10.1002/2014MS000392.

Webb, N. P., J. E. Herrick, and M. C. Duniway (2014), Ecological site-based assessments of wind and water erosion: Informing accelerated soil erosion management in rangelands, *Ecol. Appl.*, *24*, 1405–1420, doi:10.1890/13-1175.1.

Winton, V. H. L., R. Edwards, B. Delmonte, A. Ellis, P. S. Andersson, A. Bowie, N. A. N. Bertler, P. Neff, and A. Tuohy (2016), Multiple sources of soluble atmospheric iron to Antarctic waters, *Global Biogeochem. Cycles*, *30*, 421–437, doi:10.1002/2015GB005265.

Xu, L., and J. E. Penner (2012), Global simulations of nitrate and ammonium aerosols and their radiative effects, *Atmos. Chem. Phys.*, *12*, 9479–9504, doi:10.5194/acp-12-9479-2012.

Zender, C. S., H. S. Bian, and D. Newman (2003), Mineral Dust Entrainment and Deposition (DEAD) model: Description and 1990s dust climatology, *J. Geophys. Res.*, *108*(D14), 4416, doi:10.1029/2002JD002775.